

In vivo diffusion MRI of the human heart using a 300 mT/m gradient system

Maryam Afzali^{1,2}  | Lars Mueller¹  | Sam Coveney¹  | Fabrizio Fasano^{3,4}  |
 Christopher John Evans²  | Maria Engel²  | Filip Szczepankiewicz⁵ | Irvin Teh¹  |
 Erica Dall'Armellina¹  | Derek K. Jones²  | Jürgen E. Schneider¹  

¹Biomedical Imaging Science
 Department, Leeds Institute of
 Cardiovascular and Metabolic Medicine,
 University of Leeds, Leeds, UK

²Cardiff University Brain Research
 Imaging Centre (CUBRIC), School of
 Psychology, Cardiff University, Cardiff, UK

³Siemens Healthcare Ltd, Camberly, UK

⁴Siemens Healthcare GmbH, Erlangen,
 Germany

⁵Medical Radiation Physics, Clinical
 Sciences Lund, Lund University, Lund,
 Sweden

Correspondence

Jürgen E. Schneider, Biomedical Imaging
 Science Department, Leeds Institute of
 Cardiovascular and Metabolic Medicine,
 University of Leeds, Leeds LS2 9JT, UK.
 Email: J.E.Schneider@leeds.ac.uk

Funding information

EPSRC, Grant/Award Number:
 EP/M029778/1; Wellcome Trust,
 Grant/Award Numbers: 096646/Z/11/Z,
 104943/Z/14/Z, 219536/Z/19/Z; British
 Heart Foundation, UK, Grant/Award
 Number: PG/19/1/34076

Abstract

Purpose: This work reports for the first time on the implementation and application of cardiac diffusion-weighted MRI on a Connectom MR scanner with a maximum gradient strength of 300 mT/m. It evaluates the benefits of the increased gradient performance for the investigation of the myocardial microstructure.

Methods: Cardiac diffusion-weighted imaging (DWI) experiments were performed on 10 healthy volunteers using a spin-echo sequence with up to second- and third-order motion compensation (M_2 and M_3) and $b = 100, 450,$ and 1000 s/mm² (twice the b_{\max} commonly used on clinical scanners). Mean diffusivity (MD), fractional anisotropy (FA), helix angle (HA), and secondary eigenvector angle (E2A) were calculated for $b = [100, 450]$ s/mm² and $b = [100, 1000]$ s/mm² for both M_2 and M_3 .

Results: The MD values with M_3 are slightly higher than with M_2 with $\Delta MD = 0.05 \pm 0.05$ [$\times 10^{-3}$ mm²/s] ($p = 4e - 5$) for $b_{\max} = 450$ s/mm² and $\Delta MD = 0.03 \pm 0.03$ [$\times 10^{-3}$ mm²/s] ($p = 4e - 4$) for $b_{\max} = 1000$ s/mm². A reduction in MD is observed by increasing the b_{\max} from 450 to 1000 s/mm² ($\Delta MD = 0.06 \pm 0.04$ [$\times 10^{-3}$ mm²/s] ($p = 1.6e - 9$) for M_2 and $\Delta MD = 0.08 \pm 0.05$ [$\times 10^{-3}$ mm²/s] ($p = 1e - 9$) for M_3). The difference between FA, E2A, and HA was not significant in different schemes ($p > 0.05$).

Conclusion: This work demonstrates cardiac DWI in vivo with higher b -value and higher order of motion compensated diffusion gradient waveforms than is commonly used. Increasing the motion compensation order from M_2 to M_3 and the maximum b -value from 450 to 1000 s/mm² affected the MD values but FA and the angular metrics (HA and E2A) remained unchanged. Our work paves the way for cardiac DWI on the next-generation MR scanners with high-performance gradient systems.

KEYWORDS

cardiac diffusion MRI, higher-order motion compensation, strong gradients

Maryam Afzali and Lars Mueller contributed equally to this work

This is an open access article under the terms of the [Creative Commons Attribution](https://creativecommons.org/licenses/by/4.0/) License, which permits use, distribution and reproduction in any medium, provided the original work is properly cited.

© 2024 The Authors. *Magnetic Resonance in Medicine* published by Wiley Periodicals LLC on behalf of International Society for Magnetic Resonance in Medicine.

1 | INTRODUCTION

Diffusion MRI sensitizes the MR signal to the random motion of water molecules in tissue.¹ By probing the water motion in tissue, one can infer information about the underlying microstructure.² The heart is arguably one of the most challenging organs for diffusion MRI because of cardiac and respiratory motion. Macroscopic motion can cause significant signal loss and therefore dedicated motion-compensation techniques are required to scan the beating heart.^{3,4}

Cardiac diffusion-weighted MR images can be obtained free breathing using a spin-echo (SE) sequence⁵ which allows the acquisition within one cardiac cycle. However, SE cardiac diffusion-weighted imaging (DWI) with traditional monopolar encoding is sensitive to cardiac motion which changes phase coherence and can be mistaken for diffusion. One solution to this problem is to use motion-compensated diffusion-encoding gradient waveforms that are sensitive to diffusion motion and insensitive to bulk motion.³

Nulling the first moment of diffusion gradients (M_1 -nulling) to achieve velocity-compensation was first introduced for SE cardiac DWI by Gamper et al.³ Throughout this paper, M_n means all moments lower than n are also nulled. More recently, diffusion gradients with moments nulled up to the second order (M_2 -nulling), providing both velocity and acceleration compensation, have been used.^{6,4,7} Velocity and acceleration-compensated methods are presently the most common approach for SE cardiac DWI in human hearts where echo times (TEs) of 65–77 ms at a maximum b -value of 350–500 s/mm² (maximum gradient strength of 80 mT/m) have been reported.^{8–10}

The total duration of any moment-nulled gradient waveform is longer than the one of monopolar waveforms. As a result, motion-compensated waveforms increase the TE which reduces the signal-to-noise-ratio (SNR). Up to third-order motion compensation, that is, jerk-nulling (M_3 -nulling), has so far only been explored in rat hearts on a preclinical MRI scanner.¹¹

Unsurprisingly, most of the in vivo human, second-order motion compensated (M_2) SE cardiac DWI studies so far are limited to a maximum b -value of 500 s/mm² to keep the TE within a reasonable range (TE < 80 ms). However, by increasing the b -value the sensitivity of the diffusion-weighted signal to smaller spatial scales increases,¹² which allows to probe tissue microstructure of the heart.¹³ The advantage of using higher b -values is shown in several cardiac DWI ex vivo studies.^{13,14} The work from Teh et al.¹⁵ on in vivo human heart suggested that higher b -values may be advantageous in inferring microstructural information from cardiac tissue.

Improved gradient performance allows for shorter diffusion gradient waveforms (at a given b -value) and, therefore, shorter TEs, which in turn reduces signal losses from T2 relaxation.^{16–19} The Connectom MR system^{16,17} features magnetic field gradients four to eight times stronger than those on commonly available clinical MR scanners. The Connectom MR scanner has significantly reduced the resolution limit for axon diameter estimation in the brain or drastically improved the microstructural anisotropy assessment (see Reference 20 for details). Thus, similar to these neuro applications, the increased gradient performance can be expected to give new insights into cardiac microstructure. This scanner therefore also represents an opportunity to investigate the effect of higher-order motion compensation in the human heart in vivo.

Here, we demonstrate cardiac DWI investigations of the human heart on a Connectom MR system. In addition, we sought to establish the feasibility of applying third-order motion-compensated (M_3) diffusion gradients at $b_{\max} = 1000$ s/mm², which would result in prohibitively long TEs in conventional clinical MR scanners. The main focus of this work is to compare motion compensations up to second versus up to third-order (M_2 vs. M_3) and low versus high b -value ($b_{\max} = 450$ s/mm² vs. $b_{\max} = 1000$ s/mm²).

2 | METHODS

2.1 | Experimental setup and recruitment

Cardiac diffusion-weighted images were acquired on a Connectom 3T research-only MR imaging system (Siemens Healthcare) with a maximum gradient strength of 300 mT/m and slew rate of 200 T/m/s. An 18-channel body receive coil was used in combination with a 32-channel spine receive coil. Ten healthy (no known previous cardiac conditions) volunteers were recruited for this study (age range 19–36 years old (24.1 ± 6.4 years old), weight range of 54.9–112 kg (72.6 ± 20.5 kg), six females and four males). The studies were approved by the Cardiff University School of Psychology Ethics Committee and all subjects provided written consent.

2.2 | Gradient waveform design

Traditional motion-compensated diffusion encoding gradient waveforms comprise trapezoidal gradient waveforms which are (anti-)symmetric around the 180° radiofrequency (RF) pulse.^{3,11} However, spin-echo echo-planar

imaging (SE-EPI) introduces dead times before the refocusing pulse, therefore, it is more efficient to design asymmetric waveforms.^{21–23} Asymmetric waveforms are prone to concomitant fields²⁴ which can have a severe effect on the signal. To mitigate against this confounder, we consider Maxwell compensation in our waveform design.²⁵ The Maxwell compensated waveform necessitated in our case an increase of the TE by 4–6 ms (this correction may not always be essential but it becomes more important for higher gradient amplitudes since the concomitant fields scale with G^2).

Diffusion gradient waveforms were designed using the NOW toolbox^{26,27} (<https://github.com/jsjol/NOW>) to provide Maxwell-compensated waveforms that can reach a specified b -value in the shortest TE.

The waveform design was performed offline. For designing the waveform, we determined—the timing before the 180° pulse, the duration of the 180° pulse, the time after the 180° pulse, G_{\max} , SR_{\max} , and order of motion compensation, respectively. During the optimization, the encoding time was discretized into 77 (the default value in the toolbox) timesteps (of equal length), and the gradient amplitude varied at the time points to achieve the highest b -value under the following constraints: (i) linear shape of the b -tensor (gradients along a single axis); (ii) slew rate of less than 80 T/m/s to remain within the MR scanner-imposed stimulation limits (see Table S1 and Figures S3, S4, and S5, for more details); (iii) maximum gradient amplitude less than 300 mT/m; (iv) Maxwell compensation²⁵ (see Figure S7, for more details); and (v) the gradient moments up to the desired order should be smaller than a threshold (10^{-4} in unit of s^n/m , where n is the motion compensation order²⁷). The maximum b -value, in this work, was 1000 s/mm^2 , and other b -values were achieved by scaling the gradient amplitudes while keeping the shape and timing constant. It is more SNR efficient to design the waveforms for each b -value separately.

However, some part of our work is focused on comparing the effect of maximum b -value on the estimated diffusion metrics ($b = [100, 450]$ s/mm^2 vs. $b = [100, 1000]$ s/mm^2). We therefore considered it as important to avoid any contribution from TE difference, and kept the TE constant for both $b = [100, 450]$ s/mm^2 versus $b = [100, 1000]$ s/mm^2 scenarios. The waveforms with up to second- (M_2) and third-order (M_3) motion compensation are asymmetric in time and shape as shown in Figure 1. Our waveforms are not constrained a priori to a specific shape (i.e., trapezoidal, sinusoidal, etc.) since limiting the shape of the waveform makes the design suboptimal (see Figure S7). The waveforms in Figure 1 do not reach G_{\max} in the left side of the waveform, due to the Maxwell-compensation constraint. If we release this constraint, the waveform gets closer to the G_{\max} on either side of the refocusing pulse. Since the NOW toolbox does not guarantee a global minimum the optimization is repeated 10 times with random waveforms for initialization (Figure S9) and the result with the highest b -value is selected (see References 26 and 27 for more details). The NOW toolbox provides the waveforms as text files that can be read by the sequence. The sequence interpolates the gradient waveforms linearly to the raster time that is used by the scanner. This interpolated waveform is used to calculate the b -value. A potentially remaining zeroth-order moment, due to the interpolation, is compensated by adding a short, small balancing gradient pulse. The optimization processing time was on the order of minutes.²⁶

2.3 | Data acquisition

Routine GRE and TRUEFISP sequences were used for cardiac planning and cine-imaging, whereas cardiac DWI was performed with a prototype pulse sequence that enabled

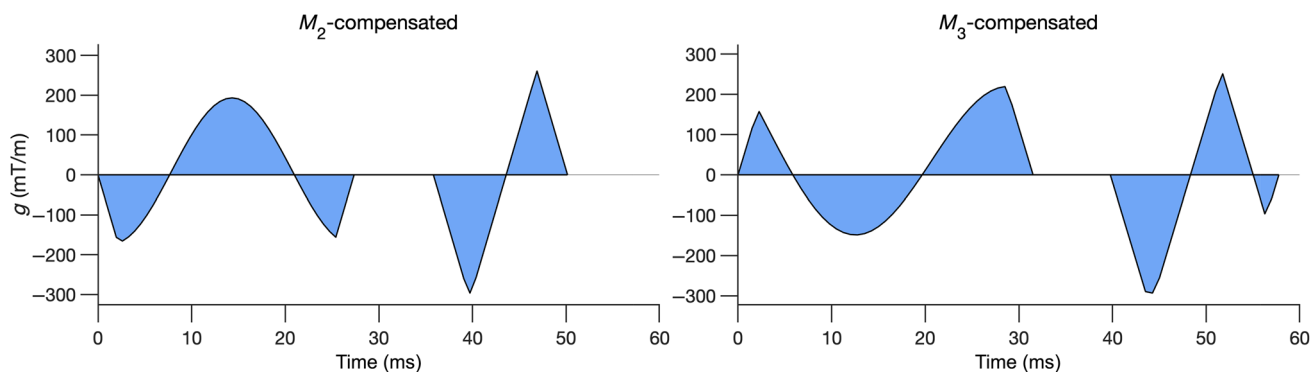


FIGURE 1 Numerically optimized motion compensated waveforms up to second- and third-order motion compensation (M_2 and M_3). The waveforms are optimized for $b_{\max} = 1000$ s/mm^2 , $G_{\max} = 300$ mT/m and maximum slew rate of 80 T/m/s (see Table S1 for more details).

diffusion encoding with user-defined gradient waveforms and with EPI readout.²⁸ The cine images were acquired in short-axis orientation for apical, mid, and basal slices. DWI was performed at the same location and orientation as the cine imaging. The phase encoding direction was systematically varied in scout DW images (step size of 30°) and the phase encoding orientation providing the best image quality was chosen for the full cardiac DWI acquisition in each subject. The cardiac DWI parameters were: TR = 3RR-intervals, field-of-view = 320 × 195 mm², in-plane resolution = 2.3 × 2.3 mm², slice thickness = 8 mm, three short axis slices (base, mid, and apical), partial Fourier factor = 7/8, no parallel imaging, bandwidth = 2012 Hz/pixel and local subject-specific shimming. Each full data set comprised of $b = 100, 450, \text{ and } 1000 \text{ s/mm}^2$ in 3, 30, and 30 directions with 12, 6, and 6 repetitions, respectively, for both M_2 and M_3 . Data were acquired with ECG-gating and under free-breathing.⁸ Neither respiratory navigation nor respiratory gating were used. Navigators can prolong the acquisition time significantly as they depend on the navigator efficiency. It is common practice to exclude motion-corrupted diffusion-weighted images in post-processing prior to diffusion tensor fitting given that the image space is oversampled with respect to number of diffusion encoding directions and repetitions. Importantly, we previously did not find any difference in diffusion biomarkers in using this approach versus data acquired with respiratory navigator (unpublished data). The latter approach came at the expense of significantly prolonged acquisition times. Saturation bands were placed around the heart to suppress the signal from outside the volume of interest. Fat suppression was performed using the SPAIR method.²⁹ The trigger delay was defined as ~20% of end-systole as determined from the cine images to acquire the images at peak systole, that is, maximal wall thickness. The total acquisition time was around one hour. Both magnitude and phase data were collected and used to generate complex-valued images. The data associated with this paper are available from the University of Leeds Data Repository, <https://doi.org/10.5518/1511>.

The maximum gradient strength used in this study for acceleration-compensation acquisition (M_2) to generate the b -value of 1000 s/mm² was 296.4 mT/m and the maximum slew-rate was 80 T/m/s which resulted in an TE of 74 ms. For the third-order motion compensation (M_3), the maximum gradient strength was 293.2 mT/m with a maximum slew-rate of 79.2 T/m/s to provide the b -value of 1000 s/mm² with the TE of 80 ms.

Separate noise-only data sets (magnitude and phase) were acquired using the same sequence without RF pulses³⁰ and with a TR of 730 ms.

2.4 | Data analysis

The phase variation in each complex-valued diffusion-weighted image was removed using the method proposed by Eichner et al.³¹ An in-house developed toolbox was used for further postprocessing.³²⁻³⁴ Real-valued diffusion-weighted images were first registered: for each slice, all low b -value images were registered to one user-specified low b -value image, and then all images were registered to the mean of the co-registered low b -value images. The two-dimensional registration was performed with SimpleElastix,³³ with rigid transformation, separately for basal, middle, and apical slices. Next, an outlier rejection technique was used to remove the outliers (e.g., the images with misregistration or motion corruption) from the data.³² Last, the diffusion tensor was fitted using weighted linear least squares regression³⁵ to the data, and diffusion metrics such as fractional anisotropy (FA), mean diffusivity (MD), helix angle (HA), and secondary eigenvector angle (E2A)³⁶ were extracted for each voxel.³² The left ventricle in each slice was segmented manually using an in-house developed toolbox.³² Parts of the left ventricle corrupted by susceptibility-related distortion were not included in the averaging for the global metrics. The noise level, σ , was measured as the SD of the real part of the noise data (acquired without RF pulses) in the image domain from 256 repetitions. The SNR of the data is defined as $\text{SNR} = S/\sigma$, where S is the measured signal intensity for each b -value and direction.¹⁴ The data were divided into four sets to conduct the experiments:

- M_2 with $b = 100$ and 450 s/mm²
- M_2 with $b = 100$ and 1000 s/mm²
- M_3 with $b = 100$ and 450 s/mm²
- M_3 with $b = 100$ and 1000 s/mm²

Bland–Altman plots were used to compare the diffusion metrics (FA, MD, and E2A) obtained from M_2 versus M_3 as well as $b_{\text{max}} = 450 \text{ s/mm}^2$ versus $b_{\text{max}} = 1000 \text{ s/mm}^2$. The mean value of MD, FA, and E2A in each slice was used for comparison. To determine the statistical significance between different schemes, the Wilcoxon signed-rank test was used where a p -value less than or equal to 0.05 was considered statistically significant.

3 | RESULTS

Figure 2 shows representative diffusion-weighted images averaged over six repeats of a single diffusion direction acquired with $b = 100, 450, \text{ and } 1000 \text{ s/mm}^2$ using second- and third-order motion compensation (M_2 and M_3). 2%

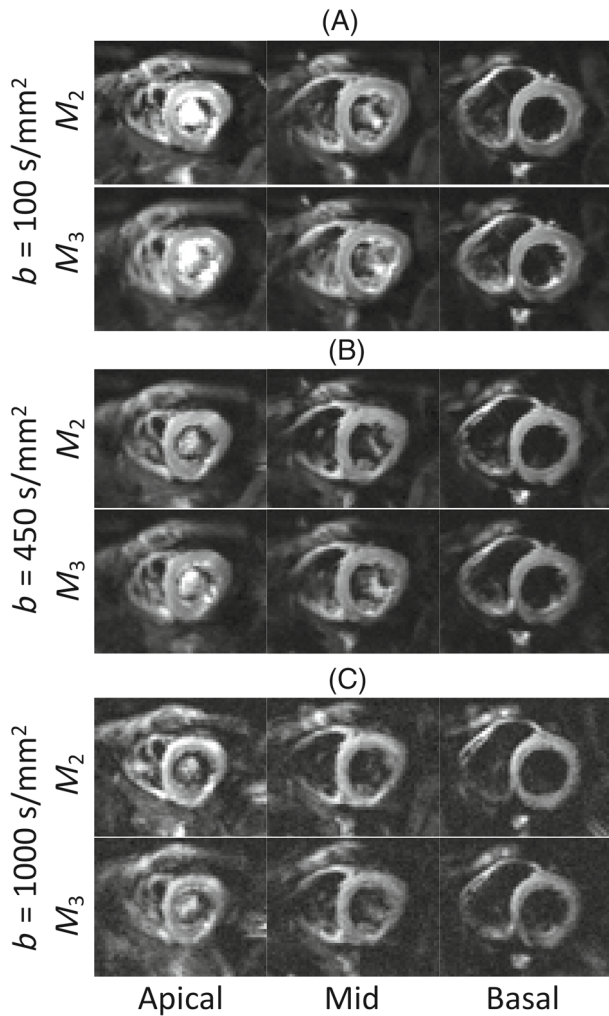


FIGURE 2 Representative cardiac diffusion-weighted images averaged over six repeats of a single diffusion direction acquired in basal, mid and apical slices with $b = 100$, 450 , and 1000 s/mm^2 (panels A–C) using second (M_2 , $\text{TE} = 74$ ms) and third-order motion compensation (M_3 , $\text{TE} = 80$ ms). M_2 - and M_3 -compensated images for each b -value are shown with the same window/grayscale level.

of diffusion-weighted images were discarded due to poor image quality and signal dropout and on average 18% of the voxels were excluded per data set for calculating the mean global metrics due to the susceptibility-related distortions. An example diffusion weighted image for each subject is shown in Figure S8. The measured SNR of the M_2 - and M_3 -compensated images at $b = 100$ s/mm^2 were 33 ± 11 , and 29 ± 10 , respectively, over the left ventricle (Figure 3). This decrease in SNR is in line with the increase in TE from M_2 ($\text{TE} = 74$ ms) to M_3 ($\text{TE} = 80$ ms), assuming a T_2 of 46 ms³⁷ ($\exp(-(\text{TE}_{M_3} - \text{TE}_{M_2})/T_2) = \exp(-6/46) \sim 0.88 \approx 29/33$). While the SNR decreases slightly going from $b = 100$ to 450 s/mm^2 , the SNR change is more pronounced from $b = 450$ to 1000 s/mm^2 (Figure 3). Each b -value uses a different window/level for better visibility.

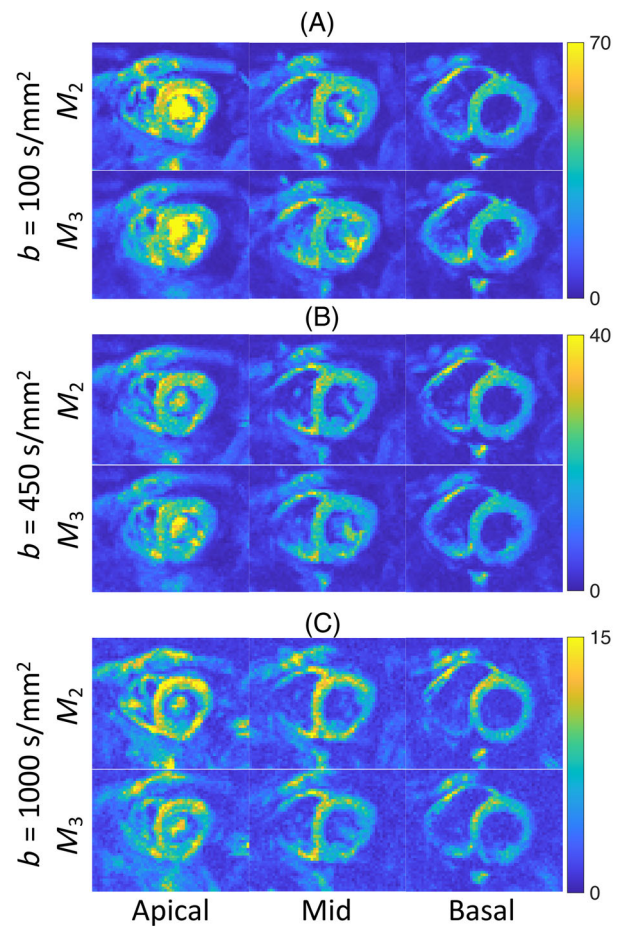


FIGURE 3 Signal-to-noise-ratio (SNR) maps obtained in basal, mid, and apical slices from a single diffusion direction (the same diffusion direction as Figure 2) with $b = 100$, 450 , and 1000 s/mm^2 (panels A–C, respectively) using second (M_2 , $\text{TE} = 74$ ms) and third-order motion compensation (M_3 , $\text{TE} = 80$ ms).

Figure 4 shows the MD, FA, E2A, and HA maps from data acquired using second- and third-order motion compensated waveforms (M_2 and M_3) with $b_{\text{max}} = 450$ s/mm^2 and $b_{\text{max}} = 1000$ s/mm^2 for three different slices. Helix angle maps obtained from acceleration-compensated diffusion encoding demonstrate the distinctive rotation from positive to negative helix angles from the subendocardium and subepicardium.³⁸ The transmural rotation of the helix angle is also apparent in the helix angle maps derived from the M_3 -compensated diffusion encoding. The mean and SD of MD, FA, and E2A for all 10 subjects are shown in Figure 5A–C. Histogram of HA values for all four schemes is shown in Figure 5D. The histograms of HA are similar for all four scenarios. The MD values are higher for $b_{\text{max}} = 450$ s/mm^2 compared to $b_{\text{max}} = 1000$ s/mm^2 for both motion compensation schemes (Table 1). The MD values are consistently higher in M_3 compared to M_2 for both b_{max} values (Table 1). There is no specific trend in FA, E2A, and HA values between different schemes.

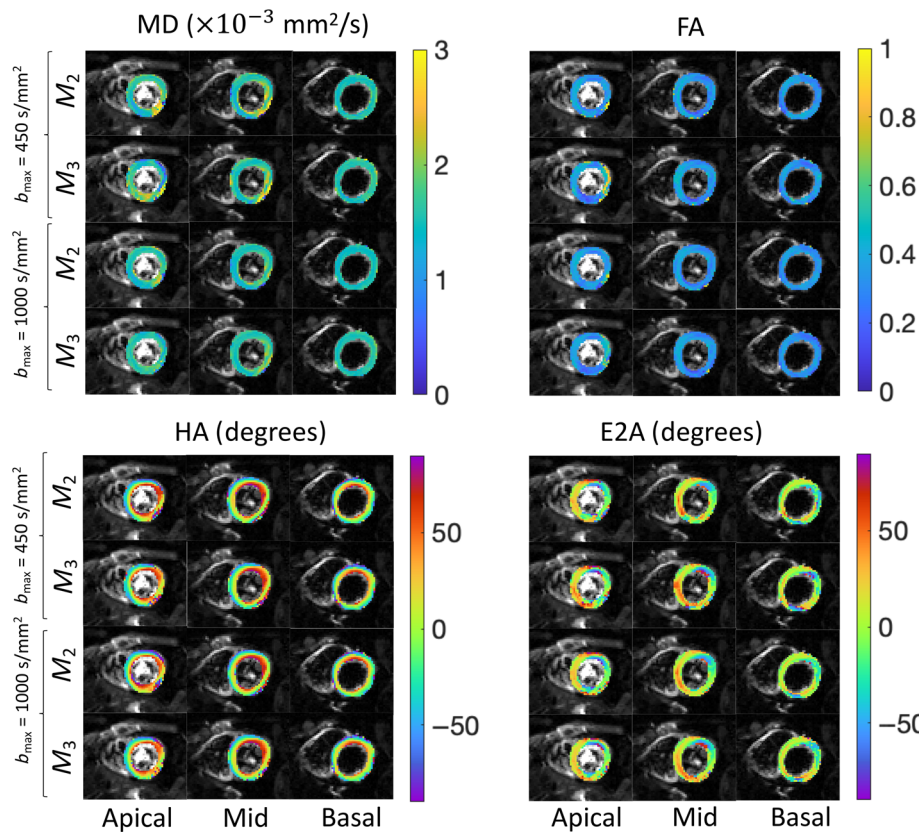


FIGURE 4 Examples of estimated mean diffusivity (MD), fractional anisotropy (FA), helix angle (HA), and secondary eigenvector angle (E2A) from data acquired using second- and third-order motion compensated waveform (M_2 and M_3) with $b_{\max} = 450 \text{ s/mm}^2$, $b_{\max} = 1000 \text{ s/mm}^2$ for basal, mid, and apical slices.

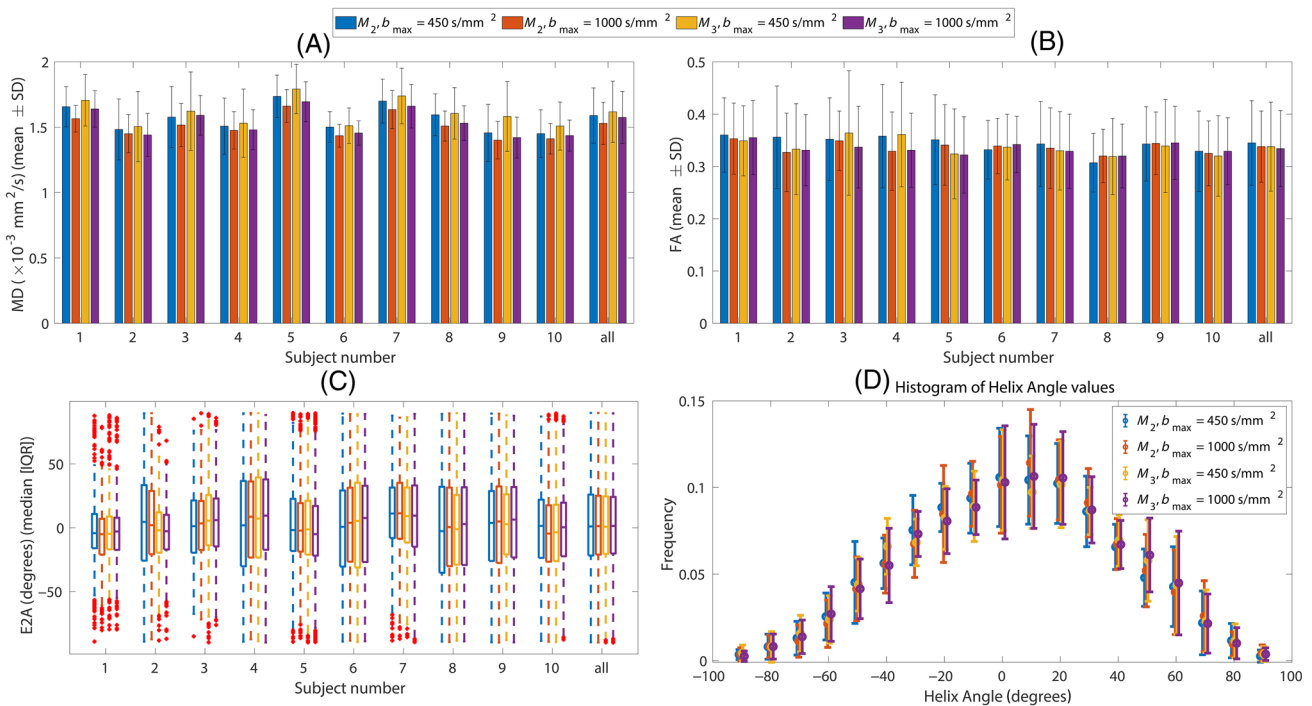


FIGURE 5 Mean and SD of (A) mean diffusivity (MD), (B) fractional anisotropy (FA), (C) median and interquartile range (IQR) for secondary eigenvector angle (E2A), and (D) histogram of helix angles (HA) over left ventricular mask. Each color shows one of the schemes. The bars shown as “all” represent the mean and SD over all 10 subjects. The red crosses in (C) show the outliers.

TABLE 1 The mean and SD of mean diffusivity (MD), fractional anisotropy (FA), and median (interquartile range [25%–75%]) secondary eigenvector angle (E2A) values inside a left ventricle mask over all three slices and over all 10 subjects.

b_{\max} (s/mm ²)		MD ($\times 10^{-3}$ mm ² /s) (mean \pm SD)	FA (mean \pm SD)	E2A (degrees) (median [IQR])
450	M_2	1.59 \pm 0.21	0.34 \pm 0.08	1 (–22 26)
	M_3	1.62 \pm 0.23	0.34 \pm 0.09	1 (–21 25)
1000	M_2	1.53 \pm 0.16	0.34 \pm 0.07	1 (–20 24)
	M_3	1.57 \pm 0.20	0.33 \pm 0.07	1 (–20 24)

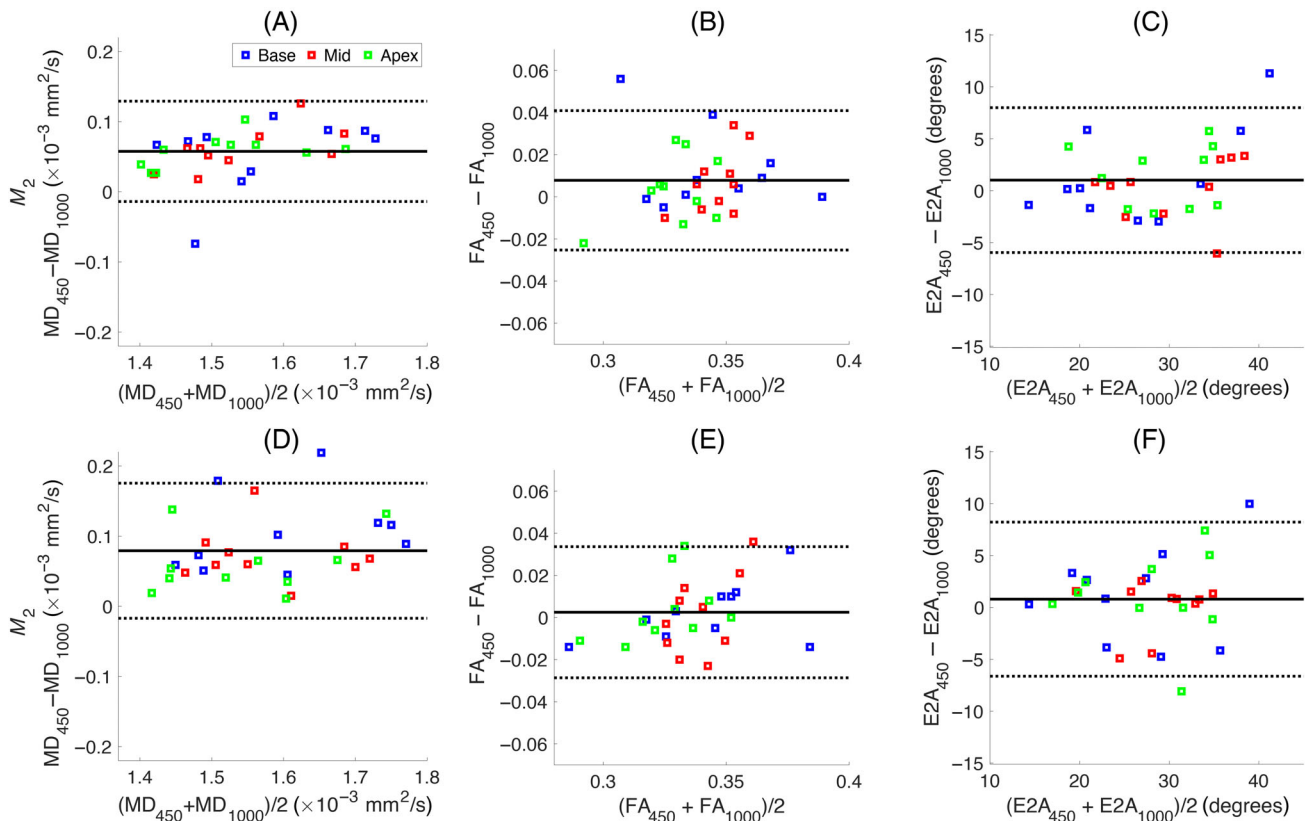


FIGURE 6 Bland–Altman plots, comparing the mean diffusivity (MD), fractional anisotropy (FA), and secondary eigenvector angle (E2A) estimated using $b_{\max} = 450$ s/mm², and $b_{\max} = 1000$ s/mm² for second- (A–C) and third-order motion compensation (D–F) (M_2 and M_3). Mean difference \pm 1.96 SD is given by solid and dashed black lines, respectively ($N = 10$ subjects). The results for basal, middle, and apical slices are shown by blue, red, and green squares, respectively. The subscripts indicate the b_{\max} that was used to estimate the metric.

To investigate the difference between diffusion metrics from different schemes further, we performed a Bland–Altman analysis, shown in Figures 6 and 7, for MD, FA, and E2A values obtained with different experimental settings. Figure 6 depicts the effect of different b -values, while Figure 7 illustrates the impact of the order of motion-compensation. The top row of Figure 6 shows the comparison between (a) MD, (b) FA, (c) E2A values obtained using $b_{\max} = 450$ s/mm² (MD_{450} , FA_{450} , and $E2A_{450}$) and the ones estimated using $b_{\max} = 1000$ s/mm² (MD_{1000} , FA_{1000} , and $E2A_{1000}$) for

the second-order motion compensation. The second row (D–F) shows the results for the corresponding comparison between $b_{\max} = 450$ s/mm² and $b_{\max} = 1000$ s/mm² for the third-order motion compensation (M_3) scheme, respectively. There is a statistically significant difference of $(0.06 \pm 0.04) \times 10^{-3}$ mm²/s ($p = 1.6e - 9$) between MD_{450} and MD_{1000} for M_2 scenario, while this difference is slightly higher for the M_3 case, $(0.08 \pm 0.05) \times 10^{-3}$ mm²/s ($p = 1e - 9$), (Table 2). The mean difference between FA and E2A from the two b_{\max} is almost negligible (Figure 6B,C,E,F). Figure 7 shows the comparison between

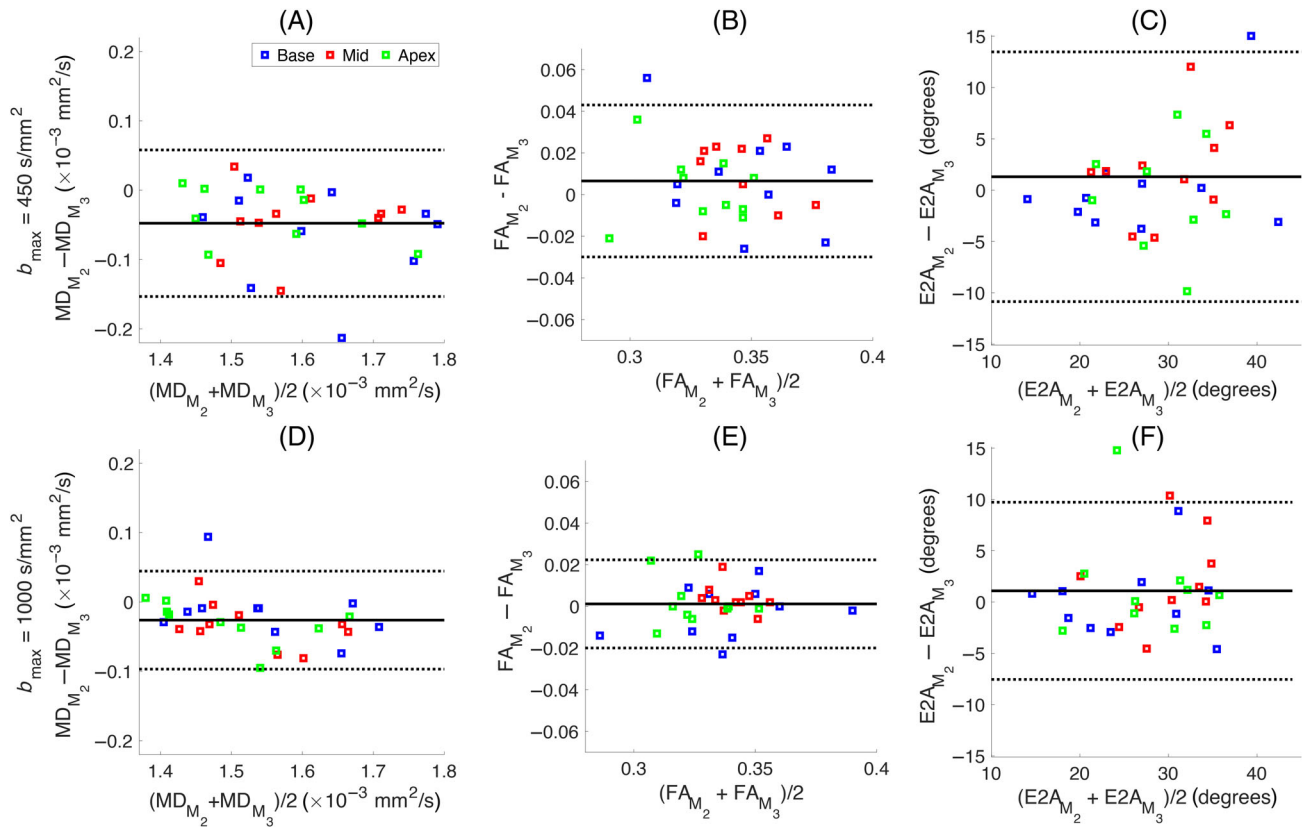


FIGURE 7 Bland–Altman plots, comparing the mean diffusivity (MD), fractional anisotropy (FA), and secondary eigenvector angle (E2A) estimated using second- and third-order motion compensation (M_2 and M_3) for $b_{\max} = 450 \text{ s/mm}^2$, (A–C) and $b_{\max} = 1000 \text{ s/mm}^2$ (D–F). Mean difference ± 1.96 SD is given by solid and dashed black lines, respectively ($N = 10$ subjects). The results for basal, middle, and apical slices are shown by blue, red, and green squares, respectively. The subscript “ M_2 ” shows the metric was obtained using second-order motion compensation and the ones with subscript “ M_3 ” are estimated using third-order motion compensation.

TABLE 2 Mean difference \pm SD of mean diffusivity (MD), fractional anisotropy (FA), and secondary eigenvector angle |E2A| inside a left ventricle mask for different schemes.

	$b_{\max} = 450$ versus $1000 \text{ (s/mm}^2\text{)}, M_2$	$b_{\max} = 450$ versus $1000 \text{ (s/mm}^2\text{)}, M_3$
$\Delta\text{MD}(\times 10^{-3} \text{ mm}^2/\text{s})$	0.06 ± 0.04 ($p = 1.6\text{e-}9$) (Figure 6A)	0.08 ± 0.05 ($p = 1\text{e-}9$) (Figure 6D)
ΔMD percentage	4%	5%
ΔFA	0.008 ± 0.016 ($p = 0.02$) (Figure 6B)	0.002 ± 0.016 ($p = 0.4$) (Figure 6E)
ΔFA percentage	2%	0.6%
$\Delta \text{E2A} (\text{degrees})$	1 ± 3 ($p = 0.13$) (Figure 6C)	1 ± 4 ($p = 0.26$) (Figure 6F)
$\Delta \text{E2A} $ percentage	4%	4%
	M_2 versus M_3 , $b_{\max} = 450 \text{ (s/mm}^2\text{)}$	M_2 versus M_3 , $b_{\max} = 1000 \text{ (s/mm}^2\text{)}$
$\Delta\text{MD} (\times 10^{-3} \text{ mm}^2/\text{s})$	-0.05 ± 0.05 ($p = 4\text{e-}5$) (Figure 7A)	-0.03 ± 0.03 ($p = 4\text{e-}4$) (Figure 7D)
ΔMD percentage	–3%	–2%
ΔFA	0.006 ± 0.018 ($p = 0.06$) (Figure 7B)	0.001 ± 0.011 ($p = 0.55$) (Figure 7E)
ΔFA percentage	2%	0.3%
$\Delta \text{E2A} (\text{degrees})$	1 ± 6 ($p = 0.26$) (Figure 7C)	1 ± 4 ($p = 0.19$) (Figure 7F)
$\Delta \text{E2A} $ percentage	4%	4%

the MD, FA, and E2A values using second- and third-order motion compensation (M_2 and M_3) for $b_{\max} = 450$ s/mm² and $b_{\max} = 1000$ s/mm². The difference between MD _{M_2} and MD _{M_3} for $b_{\max} = 450$ s/mm² was $(-0.05 \pm 0.05) \times 10^{-3}$ mm²/s ($p = 4e - 5$) which is slightly higher than the difference using $b_{\max} = 1000$ s/mm², $-0.03 \pm 0.03 \times 10^{-3}$ mm²/s ($p = 4e - 4$) (Table 2). The difference between FA and E2A obtained using M_2 and M_3 is almost negligible (Figure 7B,C,E,F).

4 | DISCUSSION

This work demonstrates the feasibility and benefits of using gradients that are much stronger than those commonly available in the clinical routine setting, for cardiac diffusion MRI applications. Conventional cardiac imaging sequences (such as cine-MRI) could be applied without any further adjustments. Using the Connectom MR system, we can reach a b -value of 1000 s/mm² with a minimum TE = 74 ms for the given imaging parameters and optimized waveforms. Notably, the same b -value on clinical routine systems with $G_{\max} = 80$ mT/m would need a TE of at least 100 ms. The approximately 25 ms shorter TE improves the SNR nearly twofold due to the short T2 of cardiac tissue: assuming a T2 of around 46 ms as reported in the literature³⁷ the SNR increase is $\exp(-74/46)/\exp(-100/46) \approx 1.76$. It can be expected that modern hard- and software (such as parallel transmit) will provide further TE savings but this was beyond the current capabilities of the Connectom MR scanner. The high-gradient amplitudes and relatively thick slices made it essential to include Maxwell compensation at only a small TE increase of 4 ms compared to the uncompensated case (see also Figure S7).

4.1 | Effect of motion compensation order (M_2 vs. M_3)

Utilizing the high-performance gradient system of the Connectom MR scanner, we were able to demonstrate third-order motion-compensated cardiac diffusion MRI with a TE of 80 ms for $b_{\max} = 1000$ s/mm² which is similar to the TE routinely used in clinical scanners for the M_2 -compensated SE-sequences at $b_{\max} = 450$ s/mm².^{9,10,8}

Previous studies demonstrated that SE (diffusion MRI) with acceleration compensated diffusion gradients (M_2) provided both sufficient SNR and insensitivity to motion (in at least the systolic phase)^{3,4,7,6} to get satisfactory cardiac diffusion images in vivo. Our work confirms this finding. However, considering that the participants in this study were healthy volunteers, with regular heartbeats, the

quality of the images acquired using M_2 and M_3 were not qualitatively different. The third-order motion compensation scheme (M_3) may result in better quality images in patients with a less regular heartbeat.

The slight difference between MD values using M_2 and M_3 could be due to the difference in the shape and timing of the diffusion gradient waveforms (Figure 1): the presence of time-dependent diffusion processes³⁹ can affect MD value estimation from second- and third-order motion compensated (M_2 and M_3) acquisitions. FA and the angular diffusion metrics (E2A and HA) were found to be the same for both motion compensation orders.

4.2 | Effect of b_{\max} (450 vs. 1000 s/mm²)

The MD and FA values using $b_{\max} = 450$ s/mm² and $b_{\max} = 1000$ s/mm² are in agreement with the results reported for cardiac DWI spin echo sequences.^{40,41,10,4,6} A reduction in MD value is observed when the b -value is increased from $b_{\max} = 450$ s/mm² to $b_{\max} = 1000$ s/mm². This reduction is statistically significant and can be attributed to non-Gaussian diffusion effects which become more pronounced at higher b -values.¹⁵ FA and HA values obtained from both b_{\max} were similar. E2A derived from both b -value data was comparable, albeit at the lower end of the range reported in the literature for SE in systole. This could be due to the timing of the DWI acquisition in the cardiac cycle. We aimed the acquisition to be in the end-systolic phase but if the timing (trigger delay) is slightly off, the data may be acquired closer to the mid-systolic phase which would result in lower E2A values.⁴²

4.3 | Limitations and future work

The diffusion-weighted technique used in our study was based on a SE EPI sequence. It is well recognized that EPI with long readouts is prone to geometrical distortions and intensity variations: off-resonance effects result in a reduced/increased encoding bandwidth in the phase-encoding direction.⁴³ These off-resonances can be caused by susceptibility-induced local gradients⁴⁴ between myocardium, deoxygenated blood, and air, which are particularly pronounced around the posterior vein.^{45,46} For the highest possible SNR, the centre of k-space should coincide with the SE condition. Since EPI does typically not follow a center-out trajectory, it prolongs TE. In addition, the minimal TE becomes dependent on imaging parameters, such as field of view, resolution, and readout bandwidth. The lack of two-dimensional RF pulses (readily available on scanners with newer software and

state-of-the-art hardware) necessitated the acquisition of a larger field of view in phase encoding direction, which increased TE further. A larger field of view in turn was necessary to avoid aliasing artifacts from signals not fully suppressed by the saturation bands. Future work will see the implementation of short, optimized multidimensional RF pulses as proposed by Vinding et al.⁴⁷ to overcome this limitation. To minimize the risk of peripheral nervous system, cardiac stimulation, and the occurrence of magnetophosphenes generated by the diffusion encoding waveforms, we compromised on the slew rate while capitalizing on the maximum gradient strength.⁴⁸ This is based on our simulations (designed waveforms in Figures S4 and S5) demonstrating that combining maximum gradient strength with the associated lower slew rate results in the shortest TE (see Figures S4 and S5, for more details). Thus, the waveforms here used a slew rate of ~ 80 T/m/s instead of 200 T/m/s theoretically possible. This added 16/14 ms to the TE of the M_2/M_3 acquisitions, respectively. Notably, using M_1 reduces the TE by 4–70 ms. We therefore opted to maintain the higher level of motion compensation.

The TE can in principle also be shortened through various complementary approaches: (1) parallel imaging techniques^{49,50} can reduce the time to the k-space center, but result in an SNR penalty. (2) inner volume imaging⁵¹ with the 90° and 180° RF pulses applied orthogonal to each other allows for a smaller FOV in phase-encoding direction, and in turn can translate into a shorter readout duration at the same spatial resolution. We refrained from implementing this technique as this will impact the three-slice acquisition protocol performed in this study. The effective TR for each slice was 3 RR intervals (i.e., approximately 3 s). Thus, acquiring the same number of slices would have resulted in threefold longer scan time (at the same T1 saturation) or caused significantly higher T1 saturation (i.e., lower SNR) at the same scan time. (3) Replacing the EPI with a spiral readout has been demonstrated to improve SNR on high-amplitude gradient systems^{18,52,53} and in cardiac DWI^{54–57} and is expected to be particularly beneficial in this context.

Reaching a b -value of 1000 s/mm² in a reasonable TE is an important achievement and opens the field for further investigations. Future work will explore non-Gaussian diffusion such as diffusion kurtosis imaging in more detail.

In this work, we only acquired the data in the systolic phase of the cardiac cycle. The main reason is that this study aimed to show the feasibility of cardiac diffusion MRI using strong gradients and spin echo based acquisitions. In addition, most of the previous spin echo based works in the literature are focused on the cardiac diffusion MRI in the systolic phase since diastolic acquisitions are challenging using SE-based sequences.⁵⁸ To make

comparisons straightforward we focused on the systolic images, but our future work will consider the cardiac diffusion MRI in the diastolic phase.

5 | CONCLUSION

We successfully demonstrated SE-based cardiac DWI acquisitions of the human heart using a Connectom scanner, which has not been performed to date. The high-performance gradients on such a scanner, which are about 4–8 \times more powerful than those available on clinical routine MR systems, enabled us to acquire cardiac diffusion-weighted images with third-order motion compensation (i.e., compensating for velocity, acceleration, and jerk) at a maximum b -value of 1000 s/mm² while achieving TEs comparable to second-order motion compensated diffusion gradients at $b = 450$ s/mm². We observed a statistically significant reduction in MD values obtained using $b = 1000$ s/mm² compared to $b = 450$ s/mm². This can be due to the non-Gaussian diffusion which is more pronounced at higher b -values and opens a new avenue for microstructural investigation of the cardiac tissue. Future work will also establish whether or not M_3 motion compensation will be sufficient to improve cardiac DWI SE acquisitions in diastole.

ACKNOWLEDGMENTS

This research was funded in whole, or in part, by Wellcome Trust Investigator Award (219536/Z/19/Z) and (096646/Z/11/Z), a Wellcome Trust Strategic Award (104943/Z/14/Z), the EPSRC (EP/M029778/1), British Heart Foundation, UK (PG/19/1/34076) and The Wolfson Foundation. For the purpose of open access, the author has applied a CC BY public copyright license to any Author Accepted Manuscript version arising from this submission. We thank Siemens Healthineers for the pulse sequence development environment. The authors would like to thank Sarah Jones for her help with data acquisition.









CONFLICT OF INTEREST STATEMENT

FS declares ownership interests in Random Walk Imaging, which holds patents related to the methodology. FF is employed by Siemens Healthineers. The remaining authors declare that the research was conducted in the absence of any commercial or financial relationships that could be construed as a potential conflict of interest.

ORCID

Maryam Afzali  <https://orcid.org/0000-0003-3378-0878>

Lars Mueller  <https://orcid.org/0000-0002-9605-9183>

Sam Coveney  <https://orcid.org/0000-0002-7134-3196>
 Fabrizio Fasano  <https://orcid.org/0000-0001-8396-4697>
 Christopher John Evans  <https://orcid.org/0000-0003-1379-3532>
 Maria Engel  <https://orcid.org/0000-0002-0143-1908>
 Irvin Teh  <https://orcid.org/0000-0002-6705-3129>
 Erica Dall'Armellina  <https://orcid.org/0000-0002-2165-7154>
 Derek K. Jones  <https://orcid.org/0000-0003-4409-8049>
 Jürgen E. Schneider  <https://orcid.org/0000-0003-0999-5684>

TWITTER

Jürgen E. Schneider  [JurgenESchneid1](https://twitter.com/JurgenESchneid1)

REFERENCES

- Basser PJ, Mattiello J, LeBihan D. MR diffusion tensor spectroscopy and imaging. *Biophys J*. 1994;66:259-267.
- Basser PJ, Pierpaoli C. Microstructural and physiological features of tissues elucidated by quantitative-diffusion-tensor MRI. *J Magn Reson*. 2011;213:560-570.
- Gamper U, Boesiger P, Kozerke S. Diffusion imaging of the in vivo heart using spin echoes—considerations on bulk motion sensitivity. *Magn Reson Med*. 2007;57:331-337.
- Stoek CT, Von Deuster C, Genet M, Atkinson D, Kozerke S. Second-order motion-compensated spin echo diffusion tensor imaging of the human heart. *Magn Reson Med*. 2016;75:1669-1676.
- Stejskal EO, Tanner JE. Spin diffusion measurements: spin echoes in the presence of a time-dependent field gradient. *J Chem Phys*. 1965;42:288-292.
- Nguyen C, Fan Z, Sharif B, et al. In vivo three-dimensional high resolution cardiac diffusion-weighted MRI: a motion compensated diffusion-prepared balanced steady-state free precession approach. *Magn Reson Med*. 2014;72:1257-1267.
- Aliotta E, Wu HH, Ennis DB. High-resolution spin-echo cardiac diffusion-weighted MRI with motion compensated convex optimized diffusion encoding (CODE). *J Cardiovasc Magn Reson*. 2016;18:P22-P26.
- das A, Kelly C, Teh I, et al. Phenotyping hypertrophic cardiomyopathy using cardiac diffusion magnetic resonance imaging: the relationship between microvascular dysfunction and microstructural changes. *Eur Heart J Cardiovasc Imaging*. 2022;23:352-362.
- Nguyen CT, Christodoulou AG, Coll-Font J, et al. Free-breathing diffusion tensor MRI of the whole left ventricle using second-order motion compensation and multitasking respiratory motion correction. *Magn Reson Med*. 2021;85:2634-2648.
- Aliotta E, Moulin K, Magrath P, Ennis DB. Quantifying precision in cardiac diffusion tensor imaging with second-order motion-compensated convex optimized diffusion encoding. *Magn Reson Med*. 2018;80:1074-1087.
- Welsh CL, DiBella EVR, Hsu EW. Higher-order motion-compensation for in vivo cardiac diffusion tensor imaging in rats. *IEEE Trans Med Imaging*. 2015;34:1843-1853.
- Jensen JH, Helpert JA. Quantifying non-Gaussian water diffusion by means of pulsed-field-gradient MRI. Paper presented at: Proceedings of the 11th Annual Meeting of ISMRM. 2003, Toronto, Canada. p2154
- Hsu EW, Buckley DL, Bui JD, Blackband SJ, Forder JR. Two-component diffusion tensor MRI of isolated perfused hearts. *Magn Reson Med*. 2001;45:1039-1045.
- McClymont D, Teh I, Schneider JE. The impact of signal-to-noise ratio, diffusion-weighted directions and image resolution in cardiac diffusion tensor imaging—insights from the ex-vivo rat heart. *J Cardiovasc Magn Reson*. 2016;19:90-100.
- Irvin T, David S, Boyle Jordan H, et al. Cardiac q-space trajectory imaging by motion-compensated tensor-valued diffusion encoding in human heart in vivo. *Magn Reson Med*. 2023;90:15-0-165
- Uğurbil K, Xu J, Auerbach EJ, et al. Pushing spatial and temporal resolution for functional and diffusion MRI in the human connectome project. *Neuroimage*. 2013;80:80-104.
- Setsompop K, Kimmlingen R, Eberlein E, et al. Pushing the limits of in vivo diffusion MRI for the human connectome project. *Neuroimage*. 2013;80:220-233.
- Wilm BJ, Hennel F, Roesler MB, Weiger M, Pruessmann KP. Minimizing the echo time in diffusion imaging using spiral readouts and a head gradient system. *Magn Reson Med*. 2020;84:3117-3127.
- Foo TKF, Tan ET, Vermilyea ME, et al. Highly efficient head-only magnetic field insert gradient coil for achieving simultaneous high gradient amplitude and slew rate at 3.0 T (MAGNUS) for brain microstructure imaging. *Magn Reson Med*. 2020;83:2356-2369.
- Jones DK, Alexander DC, Bowtell R, et al. Microstructural imaging of the human brain with a 'super-scanner': 10 key advantages of ultra-strong gradients for diffusion MRI. *Neuroimage*. 2018;182:8-38.
- Hargreaves BA, Nishimura DG, Conolly SM. Time-optimal multidimensional gradient waveform design for rapid imaging. *Magn Reson Med*. 2004;51:81-92.
- Middione MJ, Wu HH, Ennis DB. Convex gradient optimization for increased spatiotemporal resolution and improved accuracy in phase contrast MRI. *Magn Reson Med*. 2014;72:1552-1564.
- Aliotta E, Wu HH, Ennis DB. Convex optimized diffusion encoding (CODE) gradient waveforms for minimum echo time and bulk motion-compensated diffusion-weighted MRI. *Magn Reson Med*. 2017;77:717-729.
- Bernstein MA, Zhou XJ, Polzin JA, et al. Concomitant gradient terms in phase contrast MR: analysis and correction. *Magn Reson Med*. 1998;39:300-308.
- Szczepankiewicz F, Westin CF, Nilsson M. Maxwell-compensated design of asymmetric gradient waveforms for tensor-valued diffusion encoding. *Magn Reson Med*. 2019;82:1424-1437.
- Sjölund J, Szczepankiewicz F, Nilsson M, Topgaard D, Westin CF, Knutsson H. Constrained optimization of gradient waveforms for generalized diffusion encoding. *J Magn Reson*. 2015;261:157-168.
- Szczepankiewicz F, Sjölund J, Dall'Armellina E, et al. Motion-compensated gradient waveforms for tensor-valued diffusion encoding by constrained numerical optimization. *Magn Reson Med*. 2021;85:2117-2126.

28. Szczepankiewicz F, Sjölund J, Ståhlberg F, Lätt J, Nilsson M. Tensor-valued diffusion encoding for diffusional variance decomposition (DIVIDE): technical feasibility in clinical MRI systems. *PLoS One*. 2019;14:e0214238.
29. Lauenstein TC, Sharma P, Hughes T, Heberlein K, Tudorascu D, Martin DR. Evaluation of optimized inversion-recovery fat-suppression techniques for T2-weighted abdominal MR imaging. *J Magn Reson Imaging*. 2008;27:1448-1454.
30. Association National Electrical Manufacturers. *Determination of Signal-to-Noise Ratio (SNR) in Diagnostic Magnetic Resonance Imaging*. NEMA Standards Publication; 2001:1-2001.
31. Eichner C, Cauley SF, Cohen-Adad J, et al. Real diffusion-weighted MRI enabling true signal averaging and increased diffusion contrast. *Neuroimage*. 2015;122:373-384.
32. Coveney S, Kelly C, Teh I, et al. Semi-automated rejection of corrupted images in cardiac diffusion tensor imaging. Proceedings of the 32nd Annual Meeting of ISMRM. 2023. eposter 4292
33. Marstal K, Berendsen F, Staring M, Klein S. SimpleElastix: a user-friendly, multi-lingual library for medical image registration. Proceedings of the IEEE Conference on Computer Vision and Pattern Recognition Workshops. 2016:134-142.
34. Eleftherios G, Matthew B, Bagrat A, et al. Dipy, a library for the analysis of diffusion MRI data. *Front Neuroinform*. 2014;8:8.
35. Salvador R, Peña A, Menon DK, Carpenter TA, Pickard JD, Bullmore ET. Formal characterization and extension of the linearized diffusion tensor model. *Hum Brain Mapp*. 2005;24:144-155.
36. Scollan DF, Holmes A, Winslow R, Forder J. Histological validation of myocardial microstructure obtained from diffusion tensor magnetic resonance imaging. *Am J Physiol Heart Circ Physiol*. 1998;275:H2308-H2318.
37. Hanson CA, Kamath A, Gottbrecht M, Ibrahim S, Salerno M. T2 relaxation times at cardiac MRI in healthy adults: a systematic review and meta-analysis. *Radiology*. 2020;297:344-351.
38. Streeter DD Jr, Spotnitz HM, Patel DP, Ross J Jr, Sonnenblick EH. Fiber orientation in the canine left ventricle during diastole and systole. *Circ Res*. 1969;24:339-347.
39. Teh I, Coveney C, Foster RJ, et al. Time-dependent diffusion in human heart in vivo. Paper presented at: Proceedings of the 32nd Annual Meeting of ISMRM, Toronto, Canada. 2023; 344.
40. Lasić S, Szczepankiewicz F, Dall'Armellina E, et al. Motion-compensated b-tensor encoding for in vivo cardiac diffusion-weighted imaging. *NMR Biomed*. 2020;33:e4213.
41. Lasic S, Yuldasheva N, Szczepankiewicz F, et al. Stay on the beat with tensor-valued encoding: time-dependent diffusion and cell size estimation in ex vivo heart. *Front Phys*. 2022;167.
42. Khalique Z, Ferreira PF, Scott AD, et al. Diffusion tensor cardiovascular magnetic resonance in cardiac amyloidosis. *Circulation. Cardiovascular Imaging*. 2020;13:e009901.
43. Andersson JLR, Skare S, Ashburner J. How to correct susceptibility distortions in spin-echo echo-planar images: application to diffusion tensor imaging. *Neuroimage*. 2003;20:870-888.
44. Jezzard P, Balaban RS. Correction for geometric distortion in echo planar images from B0 field variations. *Magn Reson Med*. 1995;34:65-73.
45. Reeder SB, Faranesh AZ, Boxerman JL, McVeigh ER. In vivo measurement of T* 2 and field inhomogeneity maps in the human heart at 1.5 T. *Magn Reson Med*. 1998;39:988-998.
46. Meloni A, Hezel F, Positano V, et al. Detailing magnetic field strength dependence and segmental artifact distribution of myocardial effective transverse relaxation rate at 1.5, 3.0, and 7.0 T. *Magn Reson Med*. 2014;71:2224-2230.
47. Vinding MS, Skyum B, Sangill R, Lund TE. Ultrafast (milliseconds), multidimensional RF pulse design with deep learning. *Magn Reson Med*. 2019;82:586-599.
48. Molendowska M, Fasano F, Rudrapatna U, et al. Physiological effects of human body imaging with 300 mT/m gradients. *Magn Reson Med*. 2022;87:2512-2520.
49. Griswold MA, Jakob PM, Heidemann RM, et al. Generalized autocalibrating partially parallel acquisitions (GRAPPA). *Magn Reson Med*. 2002;47:1202-1210.
50. Pruessmann KP, Weiger M, Scheidegger MB, Boesiger P. SENSE: sensitivity encoding for fast MRI. *Magn Reson Med*. 1999;42:952-962.
51. Feinberg DA, Hoenninger JC, Crooks LE, Kaufman L, Watts JC, Arakawa M. Inner volume MR imaging: technical concepts and their application. *Radiology*. 1985;156:743-747.
52. Mueller L, Rudrapatna SU, Tax CMW, Wise RG, Jones DK. Diffusion MRI with b=1000 s/mm2 at TE < 22 ms using single-shot spiral readout and ultra-strong gradients: implications for microstructure imaging. Paper presented at: Proceedings of the 27th Annual Meeting of ISMRM, Montreal, QC, Canada. 2019; 0766
53. Mueller L, Afzali M, Molendowska M, et al. Boosting the SNR-efficiency of free gradient waveform diffusion MRI using spiral readouts and ultra-strong gradients. Paper presented at: Proceedings of the 29th Annual Meeting of ISMRM. 2021;0883
54. Gorodetzky M, Scott AD, Ferreira PF, Nielles-Vallespin S, Pennell DJ, Firmin DN. Diffusion tensor cardiovascular magnetic resonance with a spiral trajectory: an in vivo comparison of echo planar and spiral stimulated echo sequences. *Magn Reson Med*. 2018;80:648-654.
55. Gorodetzky M, Ferreira PF, Nielles-Vallespin S, et al. High resolution in-vivo DT-CMR using an interleaved variable density spiral STEAM sequence. *Magn Reson Med*. 2019;81:1580-1594.
56. Van Gorkum RJH, Guenther C, Koethe A, Stoeck CT, Kozerke S. Characterization and correction of diffusion gradient-induced eddy currents in second-order motion-compensated echo-planar and spiral cardiac DTI. *Magn Reson Med*. 2022;88:2378-2394.
57. Mueller L, Coveney S, Afzali M, et al. Cardiac DTI with spiral readouts with third order k-space correction but without inner volume excitation. Paper presented at: Proceedings of the 32nd Annual Meeting of ISMRM, Toronto, Canada. 2023; eposter 3613
58. Scott AD, Nielles-Vallespin S, Ferreira PF, et al. An in-vivo comparison of stimulated-echo and motion compensated spin-echo sequences for 3 T diffusion tensor cardiovascular magnetic resonance at multiple cardiac phases. *J Cardiovasc Magn Reson*. 2018;20:1-15.

SUPPORTING INFORMATION

Additional supporting information may be found in the online version of the article at the publisher's website.

Figure S1. Optimized motion compensated waveforms up to order three (M_0 , M_1 , M_2 , M_3). The waveforms were

numerically optimized with the NOW toolbox to provide the shortest echo time for $b = 1000 \text{ s/mm}^2$, $G_{\text{max}} = 300 \text{ mT/m}$, and a maximum slew rate of 80 T/m/s .

Figure S2. The percentage of magnetophosphenes perception by the participants using different motion compensation (M_0 , M_1 , M_2 , M_3) and readouts (EPI, and no readout).

Figure S3. The hardware limit, peripheral nerve stimulation, and cardiac thresholds for the G_y axis of Connectom gradient.

Figure S4. Diffusion gradient waveforms designed for $b_{\text{max}} = 1000 \text{ s/mm}^2$ and motion compensation up to the second order (M_2) for different combinations of G_{max} and maximum slew rate (S_{max}) (provided by the vendor, Figure S3 and Table S1).

Figure S5. Diffusion gradient waveforms designed for $b_{\text{max}} = 1000 \text{ s/mm}^2$ and motion compensation up to the third order (M_3) for different combinations of G_{max} and maximum slew rate (S_{max}) (provided by the vendor, Figure S3 and Table S1).

Figure S6. Predicted PNS using SAFE model for the waveforms used in this study (shown on x, y, and z axes, it is

clear that the y-axis is the most restrictive axis for the PNS threshold).

Figure S7. M_2 -compensated waveforms with different constraints and the corresponding TE.

Figure S8. Example diffusion weighted images acquired in a single direction (no averaging), with different b -values ($100, 450, 1000 \text{ s/mm}^2$) for all 10 subjects.

Figure S9. Example diffusion gradient waveforms obtained from 10 consecutive run of the optimization algorithm (NOW toolbox).

Table S1. The maximum slew-rate (S_{max}) allowed by the system for each G_{max} (provided by the vendor, Figure S3) with the corresponding minimum echo time for second- and third-order motion compensation (M_2 and M_3).

How to cite this article: Afzali M, Mueller L, Coveney S, et al. In vivo diffusion MRI of the human heart using a 300 mT/m gradient system. *Magn Reson Med.* 2024;1-13. doi: 10.1002/mrm.30118